Spectral-Feature Classification of Oceanographic Processes Using an Autonomous Underwater Vehicle

Yanwu Zhang, *Member, IEEE*, Arthur B. Baggeroer, *Fellow, IEEE*, and James G. Bellingham

***Abstract*—The paper develops and demonstrates a method of classifying oceanographic processes using an autonomous-underwater vehicle (AUV). First, we establish the "mingled-spectrum principle" which concisely relates observations from a moving platform to the frequency-wavenumber spectrum of the surveyed process. This principle clearly reveals the role of the AUV speed in mingling time and space. An AUV can distinguish between oceanographic processes by jointly utilizing temporal and spatial information. A parametric tool for designing an AUV spectral classifier is then developed based on the mingled-spectrum principle. An AUV's controllable speed tunes the separability between the mingled spectra of different processes. This property is the key to optimizing the classifier's performance. As a case study, AUV-based classification is applied to distinguish ocean convection from internal waves. It is demonstrated that at a higher AUV speed, convection's distinct spatial feature is highlighted to the advantage of classification. Finally, the AUV classifier is tested by the Labrador Sea Convection Experiment of February 1998. We installed an Acoustic Doppler Velocimeter in an AUV and it measured flow velocity in the Labrador Sea. Based on the vertical flow velocity, the AUV-based classifier captures convection's occurrence. This finding is supported by other oceanographic observations in the same experiment.**

***Index Terms*—Autonomous-underwater vehicle (AUV), classification, oceanographic process, spectral feature.**

I. Introduction

ONE of the most challenging tasks in observing and studying the ocean's temporal and spatial variability is to identify the underlying ocean process. The paper develops and demonstrates a method of classifying ocean processes using observations from an autonomous-underwater vehicle (AUV) [1].

Eulerian and Lagrangian platforms are representative of traditional oceanographic monitoring tools [2]. An Eulerian platform is fixed in location, providing time series records of measured quantities. Moored current meters and conductivity-temperature depth (CTD) sensors have become a routine in oceanographic monitoring. A Lagrangian platform, on the other hand, drifts with the current flow. By tracking Lagrangian platforms acoustically (e.g., SOFAR drifters) or by satellite (e.g., the ARGOS system) for surface floats, we can obtain a first-order description of the global ocean circulation [3], [4].

Classification imposes a higher level of requirement than monitoring. To optimize classification, both temporal and spatial features should be utilized. Eulerian and Lagrangian platforms have inherent limitations in this respect. Eulerian measurement is confined to a fixed location. Although a mooring may sense some information of the field's spatial variation via a horizontal advective current, this kind of sensing is uncontrolled and tends to be ambiguous. Deploying an array of moorings can add in spatial coverage, but high cost would often deter dense spatial sampling. A Lagrangian platform drifts with zero relative velocity against the ambient flow. It does move, but its motion is no different from the advecting current. As a drifter is bound to a tagged parcel of water, it has hardly any chance to catch sight of the real spatial variation of the field.

Since Eulerian or Lagrangian platforms have limitations in providing temporal plus spatial features of ocean processes, we resort to moving platforms with the intent to overcome this deficiency. A towed platform is tied to a surface ship. This type of platform is typically confined to a depth of no more than a few hundred meters [5]. A larger depth slows the tow speed, limits maneuverability, and increases the cost of the cable and winch system.

An AUV [1] is an unmanned, untethered moving platform. An Odyssey IIB AUV, as shown in Fig. 1, can dive to the full ocean depth in most places. Its speed range is from 0.25 to 2.5 m/s (the lower limit is for maintaining the vehicle's controllability). Once equipped with a classification capability, an AUV has the promise of autonomously searching for oceanographic processes of interest. An AUV is neither Eulerian nor Lagrangian, but cruises through the ocean at a controllable and flexible speed, collecting information in both time and space. AUV measurements thus mingle temporal and spatial variations of the sampled field. We establish the mingled-spectrum principle in Section II.

According to the mingled-spectrum principle, an AUV can distinguish between oceanographic processes by jointly utilizing temporal and spatial information. Our goal is not to reconstruct the field [6]–[9] or its original spectrum [10], but to classify the fields by the difference between their respective mingled spectra acquired by an AUV. Hence, we are to utilize the mingling of time and space to the advantage of classification, rather than regarding the mingling as a contaminating factor [11]. In Section III, we develop a parametric tool for designing an AUV-based classifier. It is shown that an AUV's controllable speed tunes the separability between the mingled

Manuscript received September 30, 2000; revised July 1, 2001. This work was supported in part by the Office of Naval Research (ONR) under Grant N00014-95-1-1316 and Grant N00014-97-1-0470, in part by the MIT Sea Grant College Program under Grant NA46RG0434, and in part by the Ford Professorship of Ocean Engineering.

Y. Zhang is with Aware Inc., Bedford, MA 01730, USA (e-mail: yanwu@alum.mit.edu).

A. B. Baggeroer is with the Department of Ocean Engineering and the Department of Electrical Engineering and Computer Science of the Massachusetts Institute of Technology, Cambridge, MA 02139 USA.

J. G. Bellingham is with the Monterey Bay Aquarium Research Institute, Moss Landing, CA 95039 USA.

Publisher Item Identifier S 0364-9059(01)09919-8.

Fig. 1. An Odyssey IIB AUV being recovered after operations.

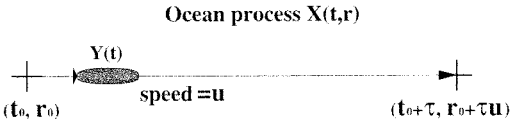

Fig. 2. A line AUV survey.

spectra of different processes. This property is the key to optimizing the classifier's performance. In Section IV, we present a test case for AUV-based classification: ocean convection versus internal waves. At last, the AUV-based classifier is tested by the 1998 Labrador Sea Experiment data, as given in Section V.

II. Mingled-Spectrum Principle

A. Mingled Spectrum Recorded by a Moving Platform

An oceanographic process varies both in time and space. We assume that a studied process is temporally stationary and spatially homogeneous. Then, the oceanographic field can be described by its frequency -wavenumber spectrum. When an AUV (or some other moving platform) carries out a survey in the field, it records a time series of some measured quantity, e.g., flow velocity. The time-series mixes temporal and spatial variations of the surveyed field. The corresponding spectrum therefore mingles the spectral information of time and space, hence we call it a "mingled spectrum".

An elementary survey mode is along a line, as illustrated in Fig. 2. Consider a scalar process X under survey. Denote its variation on the survey line as $X(t,r)$, where t is time and r is location. Denote the time series recorded by the AUV as $Y(t)$, assuming no sensor error. At an AUV speed of u, the autocorrelation function of $Y(t)$ is related to that of $X(t,r)$ by

$$\begin{aligned} R_Y(\tau) &= E[Y(t_0)\cdot Y(t_0+\tau)] \\ &= E[X(t_0,r_0)\cdot X(t_0+\tau, r_0+u\tau)] \\ &= R_X(\tau, u\tau). \end{aligned} \tag{1}$$

Under the assumptions of temporal stationarity and spatial homogeneity, we apply the Wiener-Khinchine theorem [12]. The power spectrum density (PSD) of $Y(t)$, i.e., the mingled spectrum, is the Fourier transform of $R_Y(\tau)$

$$\begin{aligned} S_Y(f)|_u &= \int_{-\infty}^{\infty} R_Y(\tau) e^{-j2\pi f\tau} d\tau \\ &= \int_{-\infty}^{\infty} R_X(\tau, u\tau) e^{-j2\pi f\tau} d\tau \end{aligned} \tag{2}$$

where f is temporal frequency.

For the temporal-spatial process $X(t,r)$, its autocorrelation function $R_X(\tau, u\tau)$ and its PSD $S_X(\eta,\nu)$ are Fourier transform pairs (also by the Wiener–Khinchine theorem [12])

$$R_X(\tau, u\tau) = \int_{-\infty}^{\infty}\int_{-\infty}^{\infty} S_X(\eta,\nu) e^{j2\pi\eta\tau} e^{-j2\pi\nu u\tau} d\eta d\nu \tag{3}$$

where η is the temporal frequency, and $\nu = k/(2\pi)$ is the spatial frequency. Note that k is a one-dimensional wavenumber in the direction of AUV's line survey. Sign convention is in accordance with that of propagating waves [13].

Incorporating (3) into (2), we have

$$\begin{aligned} S_Y(f)|_u &= \int_{-\infty}^{\infty}\int_{-\infty}^{\infty}\int_{-\infty}^{\infty} S_X(\eta,\nu) e^{-j2\pi f\tau} e^{-j2\pi\nu u\tau} \\ &\quad \times e^{j2\pi\eta\tau} d\tau d\eta d\nu \\ &= \int_{-\infty}^{\infty}\int_{-\infty}^{\infty} S_X(\eta,\nu) d\eta d\nu \int_{-\infty}^{\infty} e^{-j2\pi\tau(f+\nu u-\eta)} d\tau \\ &= \int_{-\infty}^{\infty} d\nu \int_{-\infty}^{\infty} S_X(\eta,\nu)\delta(f+\nu u-\eta) d\eta \\ &= \int_{-\infty}^{\infty} S_X\big((f+\nu u),\nu\big) d\nu. \end{aligned} \tag{4}$$

Hence, the mingled spectrum $S_Y(f)|_u$ is the integration over ν of $S_X(\eta,\nu)$ on a line defined by $\eta = f + \nu u$, as illustrated in

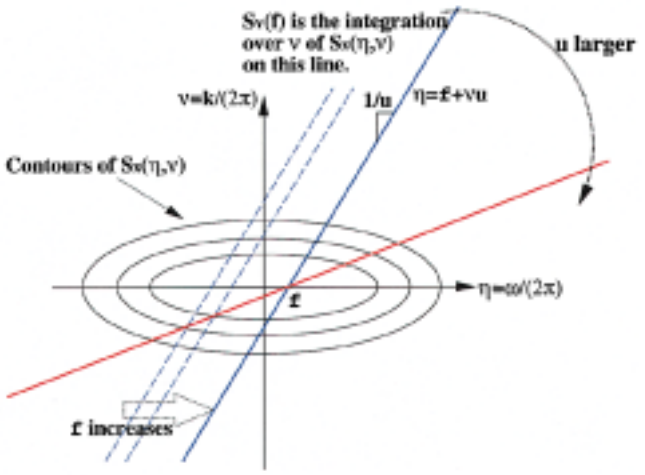

Fig. 3. Illustration of the mingled-spectrum principle. The blue line is the integration line, which intercepts with η-axis at $\eta = f$. The integration line slides from left to right to produce the mingled spectrum as a function of f. At a higher AUV speed, the red line becomes the integration line.

Fig. 3. The integration line's slope equals the reciprocal of AUV speed u. The integration line's intercept on the η-axis equals f. Equation $S_Y(f)|_u = \int_{-\infty}^{\infty} S_X\big((f+\nu u),\nu\big)d\nu$ thus concisely reveals the relationship between the "AUV-seen" mingled spectrum $S_Y(f)$ and the original temporal-spatial spectrum $S_X(\eta,\nu)$.

It can be demonstrated [14] that: 1) platform speed $u = 0$; or 2) a temporally frozen field; or 3). a nondispersive plane wave, are just several special cases under which the mingled-spectrum formula reduces to forms we are familiar with. Compared with the Doppler shifted-spectrum method [15], the mingled-spectrum principle provides advantages of applicability to isotropy or anisotropy, ease for inspection, and simplicity of computation [14].

B. Utilization for AUV-Based Classification

Let us first look at two simple fictitious temporal-spatial fields for the purpose of demonstration. Their η–ν spectra are expressed in (5) and (6), and displayed in the upper panel of Fig. 4. The η–ν spectrum of field no. 2 is just a transpose of that of field no. 1. In both spectra, the range of frequency η is from –1 to 1 Hz, while the range of wavenumber ν is from –1 to 1 m^{-1}.

$$S_{X1}(\eta,\nu) = \frac{1}{2\pi\sigma_{\eta 1}\sigma_{\nu 1}} e^{[-\eta^2/(2\sigma_{\eta 1})^2 + (|\nu|-\nu_0)^2/(2\sigma_{\nu 1})^2]} \quad (5)$$

$$S_{X2}(\eta,\nu) = \frac{1}{2\pi\sigma_{\eta 2}\sigma_{\nu 2}} e^{-[(|\eta|-\eta_0)^2/(2\sigma_{\eta 2}^2) + (\nu^2/(2\sigma_{\nu 2}^2)]} \quad (6)$$

where $\eta_0 = \nu_0 = 0.5$, $\sigma_{\eta 1} = \sigma_{\nu 2} = 0.2$, $\sigma_{\eta 2} = \sigma_{\nu 1} = 0.1$.

The spectrum of the AUV-recorded time series in a line survey is the mingled spectrum formulated in (4). The mingled spectrum, rather than the field's original frequency wavenumber spectrum, is the information source for spectral classification, because time and space are already mixed in the AUV's record. As revealed by (4) and Fig. 3, time-space mixing is tuned by the AUV speed u as the integration is constrained by a line whose slope equals $1/u$.

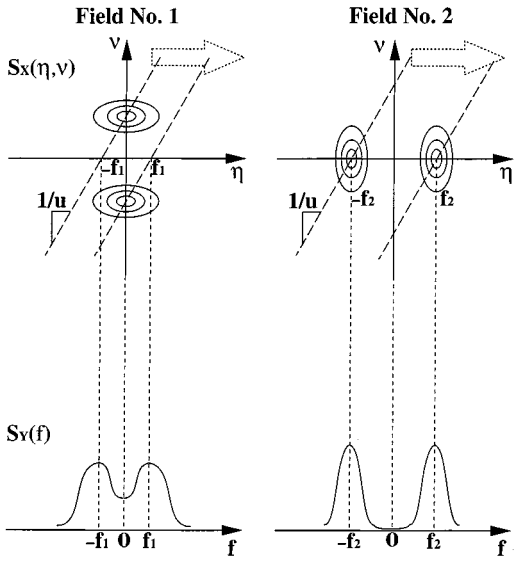

Fig. 4. Derivation of mingled spectra from the two fictitious η–ν spectra. The slanted line is the integration line, which slides from left to right to produce $S_Y(f)$.

For the above two fictitious fields, their mingled spectra as computed by (4) is illustrated in the lower panel of Fig. 4. At a series of vehicle speeds, the two mingled spectra are shown in Fig. 5. The observation is: the two mingled spectra may appear more alike or more distinct depending on the AUV's cruise speed. Due to the "transpose" relation between the two hypothesized η–ν spectra, their mingled spectra are identical when the AUV cruises at a speed of 1 m/s (the third panel of Fig. 5). This would obviously prohibit classification. At other speeds of 0.5 m/s (the second panel) and 2 m/s (the fourth panel), however, the two processes are classifiable as their mingled spectra show difference. A quantitative metric for separability will be given in Section III.

It should be noted that our goal is not trying to reconstruct the field [6]–[9] or its original spectrum [10], but to classify the fields by the difference between their respective mingled spectra acquired by an AUV. From this standpoint, we are to utilize the mingling of time and space to the advantage of classification, rather than regarding the mingling as a contaminating factor [11].

III. AUV-Based Spectral Classification

A. Classifier Architecture

The AUV-based classifier's architecture is illustrated in Fig. 6. The scope of our study is confined to two classes, denoted by H_1 and H_2 (H stands for "Hypothesis"), respectively. AUV's measurement $Y(t)$ is the input to the classifier. $Y(t)$ mingles temporal and spatial variations of the field, and its PSD $S_Y(f)$ is a mingled spectrum. It is related to the field's temporal-spatial PSD $S_X(\eta,\nu)$ by the mingled-spectrum formula (4). From AUV's measurement $Y(t)$, we obtain an estimate of its PSD, $\hat{S}_Y(f)$. Hereafter, we denote the true PSD as $S_Y(f)$ and its estimate as $\hat{S}_Y(f)$ (for class 1 and 2, footnotes "1" and "2" are added for distinction). Classification [16], [17] relies on the "distance" (i.e., the spectral separability) between

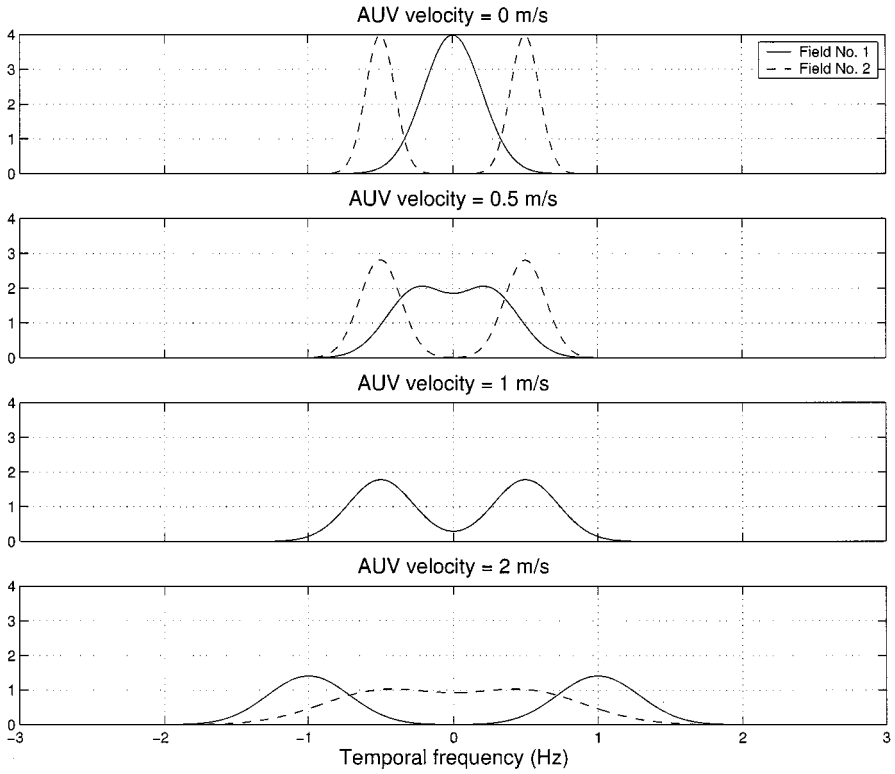

Fig. 5. Mingled spectra of the two fictitious fields.

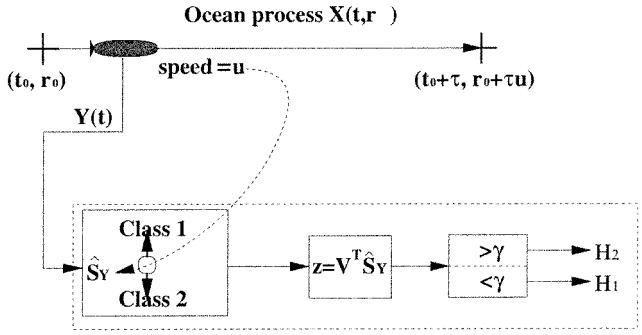

Fig. 6. Diagram of the AUV-based spectral classifier.

the two mingled spectra $S_{Y1}(f)$ and $S_{Y2}(f)$. The AUV speed tunes this distance.

We use the Fourier method of periodogram [18], [19] for spectrum estimation, so $\hat{S}_Y(f)$ is given at a series of discrete frequencies. Thus, the PSD estimate is expressed as a column vector $\hat{S}_Y(k), k = 0, 1, \ldots, N-1$, where N is the total number of frequency points. In consideration of instrument noise, there exists an upper bound of usable frequency range for classification, as will be detailed in Section IV-C.

A scalar feature z is then extracted from vector $\hat{S}_Y$ through a linear transformation

$$z = V^{\mathrm{T}} \hat{S}_Y \tag{7}$$

where V is the feature projection vector.

We adopt the Fisher's separability metric [17] to measure the "distance" between spectra in the two classes. Under this metric, it can be proven [17] that all separability information is preserved despite the N-dimension $\rightarrow$ one-dimension projection.

Finally, the scalar feature z passes a threshold comparator to make the classification decision (H_1 or H_2). The threshold γ is determined by minimizing the total cost or probability of error (the Bayesian criterion), or by satisfying some prescribed false alarm probability (the Neyman–Pearson criterion) [16].

B. Feature Projection Vector V

The feature projection vector V is clearly the key to the classifier. V is formulated as follows [17]:

$$V = A_{w\_Y}^{-1}(M_{Y2} - M_{Y1}) \tag{8}$$

where

$$M_{Yi} = E[\hat{S}_Y | H_i], \qquad i = 1, 2 \tag{9}$$

is the mean spectrum in each class and

$$A_{w\_Y} = \sum_{i=1}^{2} (P_i \Sigma_{Yi}) \tag{10}$$

is the within-class scatter matrix that depicts the scatter of $\hat{S}_Y$ around its mean spectrum in each class. P_i is the a priori probability of class i, and Σ_{Yi} is the covariance matrix in class i

$$\Sigma_{Yi} = E\left[\left(\hat{S}_Y - M_{Yi}\right)\left(\hat{S}_Y - M_{Yi}\right)^{\mathrm{T}} | H_i\right], \qquad i = 1, 2. \tag{11}$$

To help explain V's mechanism, let us consider a very simple case. Suppose vector $\hat{S}_Y$ has only two components, as

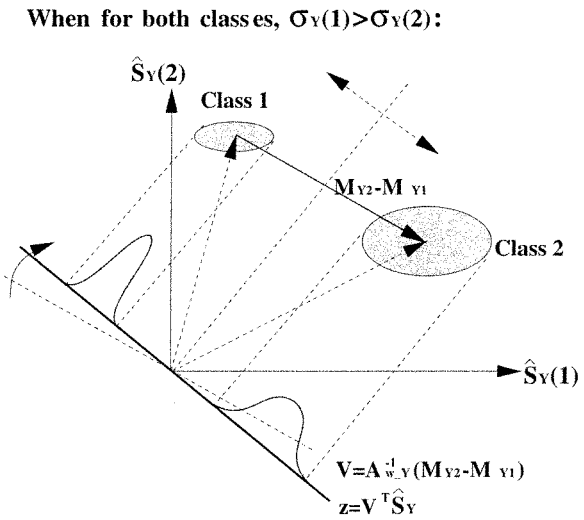

Fig. 7. Mechanism of feature projection when the two-dimensional Σ_{Yi} is diagonal with $\sigma_{Yi}(1) > \sigma_{Yi}(2), i = 1, 2$.

shown in Fig. 7. If Σ_{Yi} were diagonal with equal elements $\left(\sigma^2_{Yi}(1) = \sigma^2_{Yi}(2)\right)$, A_{w_Y} would be a scaled identity matrix and V would simply coincide with the vector of difference between the mean vectors: $M_{Y2} - M_{Y1}$. When Σ_{Yi} is still diagonal but with unequal elements: e.g., $\sigma^2_{Yi}(1) > \sigma^2_{Yi}(2)$ as shown in Fig. 7, A_{w_Y} will no longer be a scaled identity matrix but will play a role in the formation of V. As Fig. 7 illustrates, the role of A_{w_Y} is to rotate V away from the $\hat{S}_Y(1)$-axis and toward the $\hat{S}_Y(2)$-axis. This rotating represents a penalty on the $\hat{S}_Y(1)$-axis projection because the uncertainty of $\hat{S}_Y(1)$ is larger than that of $\hat{S}_Y(2)$. The separability between the two clusters of feature z is maximized using the rotated V.

To compute V, we need to know mean spectra $M_{Y1}(f)$ and $M_{Y2}(f)$, as well as covariance matrices Σ_{Y1} and Σ_{Y2} of the two processes of interest. We choose frequency points with an interval of the finite data window's bandwidth. So the PSD estimates at those frequencies are uncorrelated [19]. Covariance matrix Σ_{Yi} is consequently diagonal, where the diagonal elements are spectrum variance $\mathrm{Var}[\hat{S}_{Yi}(f)]$ at the chosen frequencies.

For each oceanographic process, we use a model to obtain its temporal-spatial PSD $S_X(\eta, \nu)$ (examples will be given in Section IV). The mingled spectrum $S_Y(f)$ is then derived from $S_X(\eta, \nu)$ by (4). We regard the resultant $S_Y(f)$ (with the additional consideration of the finite data window effect) as the mean spectrum $M_{Yi}(f)$ ($i = 1$ or 2).

The PSD estimate's variance $\mathrm{Var}[\hat{S}_{Yi}(f)]$ originates from two sources: periodogram's inherent uncertainty and model parameter uncertainty. The periodogram method [18], [19] dictates that the PSD estimate's variance is proportional to $(M_{Yi}(f))^2$, where the coefficient is determined by the settings in time-domain segmentation and frequency-domain smoothing. Model-parameter uncertainty describes possible mismatch between the model and the real data. To build the spectrum template in each class, we assign a set of parameters to the corresponding model. Those parameters are selected based on our understanding of the process and available prior information. Parameters of the real data, however, may have some discrepancy from the model's. This mismatch is referred to as parameter uncertainty. In formulating $\mathrm{Var}[\hat{S}_{Yi}(f)]$, we have taken into account both uncertainty sources. Due to space limit, the formula and its derivation are omitted. By including model parameter uncertainty in the design, the classifier is made robust to model mismatch.

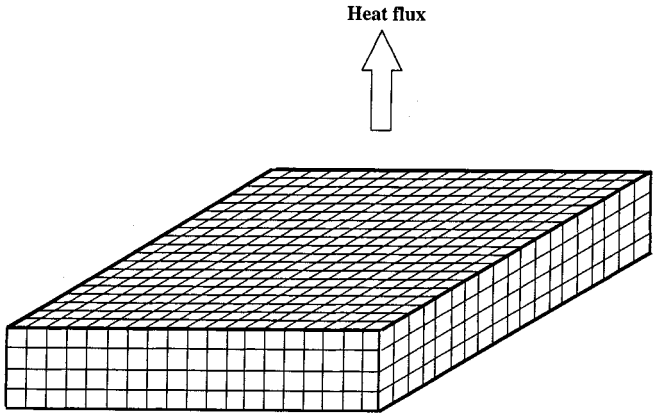

Fig. 8. Illustration of the convection model box. Only the top surface is subjected to a heat flux. The dimension is $200 \times 200 \times 35$ with a grid size of 10 m.

TABLE I
MIT CONVECTION MODEL PARAMETERS

Parameter	Symbol	Value
Initial temperature	$T_0(z)$	Labrador Sea profile
Initial salinity	$S_0(z)$	Labrador Sea profile
Surface heat flux	Q	300 W/m^2
Initial velocities	u_0, v_0, w_0	0
Grid length	Δx, Δy, Δz	10 m
Number of grids in x and y	N_x, N_y	200
Number of grids in z	N_z	35
Internal iteration time step	$\Delta t_{iteration}$	10 s
Data output time step	Δt_{output}	30 s

IV. Test Case: Ocean Convection Versus Internal Waves

We introduce two oceanographic processes for demonstrating AUV-based classification. They are ocean convection and internal waves. Vertical flow velocity is a key signature of both processes [20], [21]. Thus we select it as the quantity $X(t, r)$ (shown in Fig. 2) for classification. Prospects of introducing more quantities (e.g., temperature) to improve classification will be discussed in Section VI.

A. Ocean Convection

Convection is the transfer of heat by mass motion of fluid [22]. It happens when the density distribution becomes unstable [3]. Open ocean convection takes place at only a few locations around the world, namely, the Labrador Sea [23], the Greenland Sea [20], Mediterranean [21], and around the Antarctica [24]. At those locations, strong winter cooling of the surface water

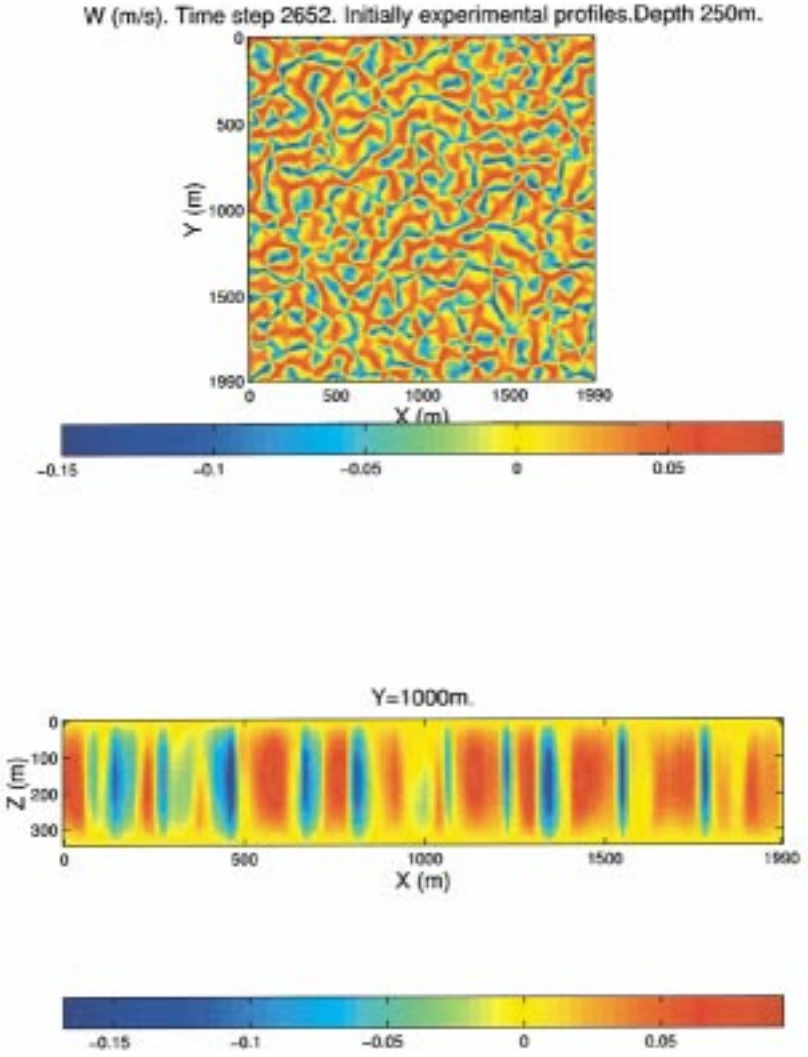

Fig. 9. Horizontal and vertical cross sections of convective vertical flow velocity w at time 7.4 h. Unit of horizontal bars is m/s.

causes it to become denser than the water beneath. The cooled surface water sinks and mixes with deeper water which enters the global ocean circulation. This process releases heat from the overturned water to the atmosphere and thus maintains a moderate winter climate on the land. Hence, ocean convection is an important mechanism for global heat transfer [25].

Prof. John Marshall and his group at the MIT Department of Earth, Atmospheric, and Planetary Sciences have constructed a numerical model of open ocean convection [26], [27]. We use this model to find the temporal-spatial spectrum of convective vertical velocity.

The model is configured as a box as shown in Fig. 8. Water is cooled at the top surface. There is no normal heat flux at the bottom or the four side walls. The parameters of surface heat flux and mixed-layer depth are set by using the meteorological and hydrographic data acquired during AUV Mission B9 804 107 in the 1998 Labrador Sea Experiment that will be presented in Section V. It is noted that owing to consideration of model parameter uncertainty, the classifier aims to be robust to significant discrepancies between model parameters and real data parameters. Main model parameters are listed in Table I. Note that the model's dimensional scale is on the order of 1 km.

At 26 520 s (about 7.4 h) after surface cooling starts, the model output of vertical flow velocity w is shown in Fig. 9. The upper panel displays the horizontal cross section at the 250-m depth, the same depth of AUV Mission B9 804 107. The lower panel displays the vertical crosssection at $y = 1000$ m. Convective cells with periodicity of 200 m–250 m are observable in both panels.

Based on the model output for two hours (from 5.4 to 7.4 h after the onset of surface cooling), we compute the temporal-spatial PSD of convective vertical velocity w, as shown in the upper panel of Fig. 10 (while the mingled-spectrum principle does not rely on isotropy, we consider the convection field to be isotropic because of the isotropic surface cooling in the model. Based on symmetry properties, the whole η–ν spectrum is constructed using the first quadrant). Temporally, the vertical-velocity field varies little during the two-hour evolution as convection approaches a stationary state. The observed baseband spectrum on the η-axis is mostly due to the two-hour window (the Fourier transform of a boxcar window is a sinc function).

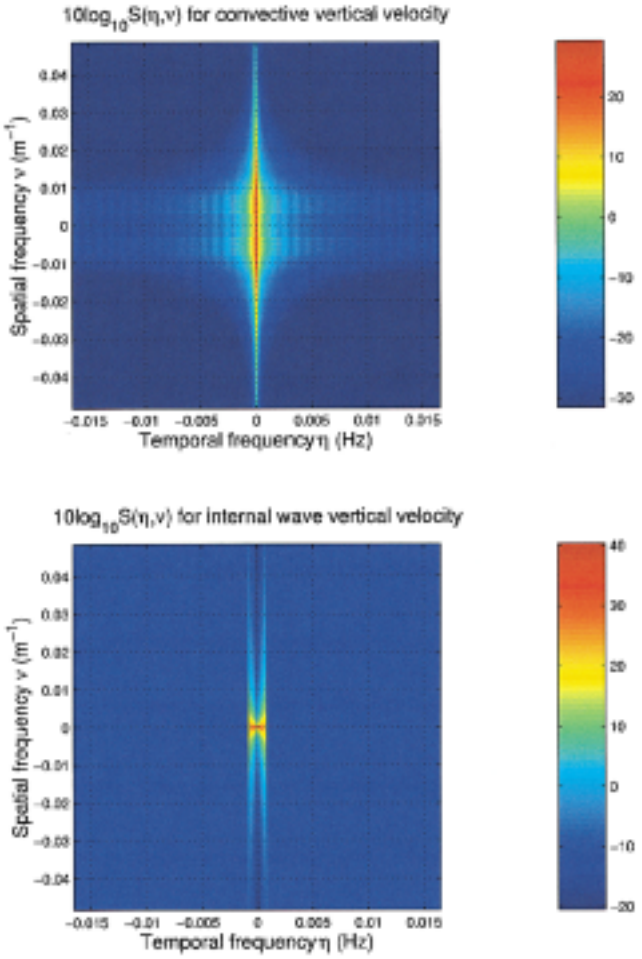

Fig. 10. Temporal-spatial PSD of vertical velocity of convection (upper) and internal waves (lower, with an extended plateau). Unit of vertical bars is $10\log_{10}((\mathrm{m/s})^2/(\mathrm{Hz}\cdot\mathrm{m}^{-1}))$.

on the ν-axis, however, there is a peak at about 0.005 m^{-1} because convective cells have a spatial periodicity of about 200 m. We can utilize the AUV's speed to highlight this feature of convection for classification against internal waves.

B. Internal Waves

Internal waves occur in the ocean's interior. It is the water's response to a disturbance to its equilibrium of hydrostatically stable density stratification, via the gravitational restoring force [28]. Unlike convection which occurs in a vertically unstable or mixed water column, internal waves are found in stably stratified water. Stable stratification is depicted by the buoyancy frequency (also called the Brunt-Vaisala frequency) [29] that is determined by the density profile.

Internal waves play an important role in mass and momentum transfer in the ocean [11]. Their dynamics is essential for understanding the ocean circulation and temperature and salinity structures [11]. In another aspect, sound-speed fluctuations induced by internal waves are a dominant source of the high-frequency variability of acoustic wave fields in the ocean [30].

Based on the Garrett-Munk model [11], [15], [31], [32], we derive the temporal-spatial PSD of internal-wave vertical velocity. The spectrum is confined within a frequency range

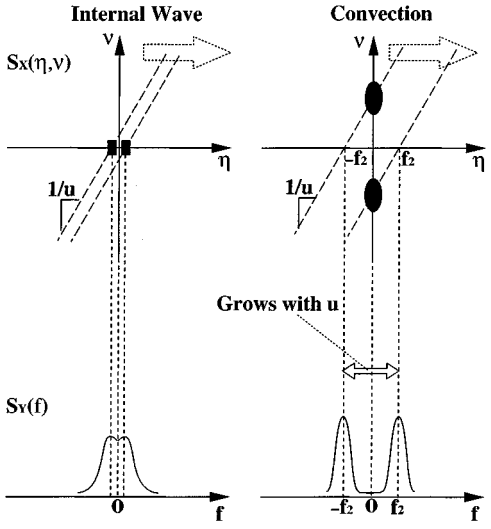

Fig. 11. Derivation of mingled spectra from temporal-spatial spectra of convection and internal wave vertical velocities.

of Coriolis frequency ($2f_{\mathrm{rot}}\sin(\phi) \approx 1.9\times10^{-5}$ Hz where $f_{\mathrm{rot}} = 1$ cycle/day is the angular velocity of Earth's rotation and $\phi \approx 57°$N is the latitude of the 1998 Labrador Sea Experiment site) and buoyancy frequency (taken as 8×10^{-4} Hz,

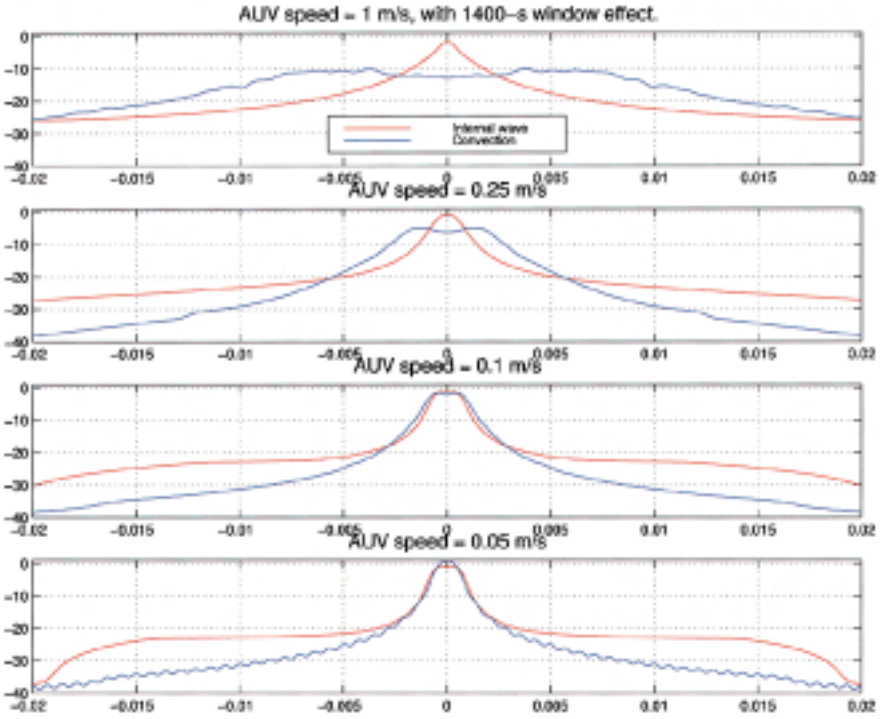

Fig. 12. Mingled spectra of vertical velocities of convection and internal waves. Abscissa is frequency in hertz; the unit of ordinate is $10\log_{10}((\text{m/s})^2/\text{Hz})$.

equivalent to nearly three cycles per hour [32]). In the ocean, however, processes of frequencies higher than the buoyancy frequency do exist [11], like turbulence [4]. We therefore need to consider higher frequency processes along with internal waves. We add a spectrum plateau above the buoyancy frequency to account for higher-frequency processes. Based on a PSD plot of ocean wave kinetic energy, we calculate the ratio $(\text{Power above buoyancy frequency}/\text{Power of internal waves})$. This ratio is then used to set the plateau's height. Although a plateau is not an accurate description of the spectrum, we deem it sufficing to serve the purpose of this case study since the forthcoming computation of mingled spectrum is in an integration sense. From the perspective of classification, the spectrum extension will prevent a classifier from unduly taking advantage of a vanishing part of a spectrum (referred to as "singular detection" [16], [33] in detection theories).

With this plateau extension above the buoyancy frequency, the temporal-spatial PSD of internal wave vertical velocity is shown in the lower panel of Fig. 10. Note that for the sake of testing the classifier, we have scaled internal wave vertical velocity's amplitude such that its power equals that of convective vertical velocity. On the ν-axis, most power lies at very low wavenumber, showing no peak away from $\nu = 0$. In contrast, the temporal-spatial PSD of convective vertical velocity has a spectral peak at about $\nu = 0.005\ \text{m}^{-1}$ due to convective cells' periodicity, as shown in the upper panel of Fig. 10. This distinction is what a cruising AUV can take advantage of for classification, as will be seen in the following.

C. Mingled PSDs at a Series of AUV Speeds

Having obtained $S_X(\eta, \nu)$ of convective and internal wave vertical velocities, let us derive the AUV-seen $S_Y(f)$ by the mingled-spectrum principle, as illustrated in Fig. 11. Convection's spatial peak on the ν-axis is projected onto the f-axis of the corresponding mingled spectrum. At a higher AUV speed, the spectral peak on the f-axis is pulled farther away from $f = 0$. For internal waves, however, the picture is different. Since internal waves' power is concentrated at baseband on the η-axis and the ν-axis, the corresponding mingled spectrum also lies at baseband on the f-axis. A higher AUV speed will not change this basic spectral shape. Based on this inspection even before conducting computations, we project that the distinction between the two spectra will enlarge with AUV speed.

We apply (4) at a series of AUV speeds $u = 1$ m/s, 0.25 m/s, 0.1 m/s, and 0.05 m/s. The resultant mingled spectra of convective and internal wave vertical velocities are compared in Fig. 12. Data window effect has been included in the calculations. The window length is set to 1400 s to coincide with that of the AUV's Labrador Sea experimental data which will be presented in Section V. The results in Fig. 12 are consistent with the predictions inspected from Fig. 11.

In consideration of instrument noise, there exists an upper bound of usable frequency range for classification. We require that across this valid frequency range, mingled spectra of both processes maintain a signal-to-noise-ratio (SNR) of 20 dB over the instrument noise floor of the acoustic Doppler velocimeter (ADV) under normal operation conditions (an AUV-borne ADV acquired the flow velocity data in the Labrador Sea Experiment, as will be presented in Section V). At a lower AUV speed, spectrum levels drop more steeply toward high frequency, thus the valid frequency range shrinks as the vehicle speed decreases. The upper bound of valid frequency range is 0.009, 0.006, 0.004, and 0.003 Hz at AUV speed $u = 1$ m/s, 0.25 m/s, 0.1 m/s, and 0.05 m/s, respectively. Taking those ranges into account, we see

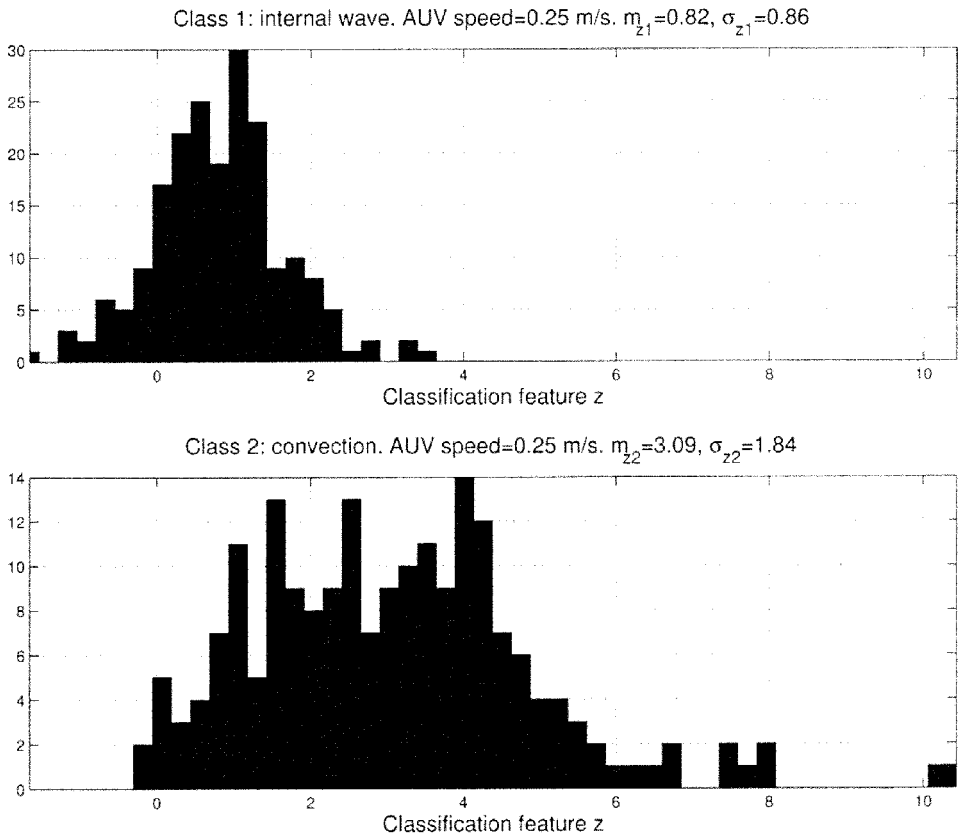

Fig. 13. Histogram of scalar feature z in class 1 (internal waves, upper panel) and class 2 (convection, lower panel) at AUV speed 0.25 m/s.

that the mingled-spectrum pairs are much more distinguishable at higher AUV speeds.

D. Classifier Test Results of Model Based Simulations

For simulating a line AUV survey in the convection field, the AUV-recorded time series is directly drawn from the convection model at depth 250 m. An ensemble of 200 AUV survey lines are used for every classifier test at each prescribed AUV speed. To add randomness to different test runs, the starting time and location are randomly picked (within range).

In the internal wave field, we simulate a line AUV survey time series by passing white noise through a first-order (at AUV speed $\geqslant 0.25$ m/s) or second-order (at AUV speed < 0.25 m/s) autoregressive (AR) model [34]. This method is suggested by the shape of the mingled spectrum: e.g., at AUV speed $\geqslant 0.25$ m/s, the mingled spectrum approximately follows a power law of f^0 at low frequency and f^{-2} at high frequency. Parameters of an AR model are selected such that its output spectrum best matches the mingled spectrum. Two hundred AUV survey lines in the internal wave field are randomly generated in every classifier test.

Now we test the classifier. For each time series of AUV data, its PSD estimate is converted to a scalar feature z by the transformation vector V following (7). For each test, 200 lines of AUV data in the convection field and another 200 lines in the internal wave field are used. Classifier performance is evaluated by the statistics of the resultant ensemble of z.

Corresponding to Fig. 12, we test the classifier at a series of AUV speeds $u = 1$ m/s, 0.25 m/s, 0.1 m/s, and 0.05 m/s. At $u = 0.25$ m/s, histograms of scalar feature z in the two classes are shown in Fig. 13. In each panel, there are 200 z values (binned). Histogram of z shows its statistical distribution. Let us define the false alarm probability P_F as that of declaring convection when internal wave is true; the detection probability P_D as that of declaring convection when convection is indeed true. The classifier's P_D–P_F relationship is depicted by the receiver operating characteristic (ROC [16]), as shown in Fig. 14. Note that the ROC curve is determined solely by the probability distribution functions of z, not by the detection threshold.

At lower AUV speeds 0.1 m/s and 0.05 m/s, histograms of scalar feature z in the two classes severely overlap (plots omitted). The corresponding ROC curves are shown in Fig. 14. We know that a lower ROC curve implies a lower classifier performance, the worst being the diagonal line which is equivalent to flipping a coin. Thus, at lower AUV speeds, classification appears to be more difficult. This is an expectable outcome by comparing the mingled spectrum pairs in Fig. 12 (also keeping in mind valid frequency ranges as given in Section IV-C). At a low vehicle speed, convection's spatial variation cannot be well sensed by the AUV, so the recorded time series is basically still low-pass, similar to an internal wave measurement.

At a higher AUV speed, convection's spatial peak on the ν-axis is apparently projected onto the f-axis of the corresponding mingled spectrum, as displayed by Fig. 11. Thus convection's spatial feature is brought to light in the AUV-recorded time series. Due to the properties of internal wave's frequency -wavenumber spectrum, its mingled spectrum lies at baseband on the f-axis. A higher AUV speed does not

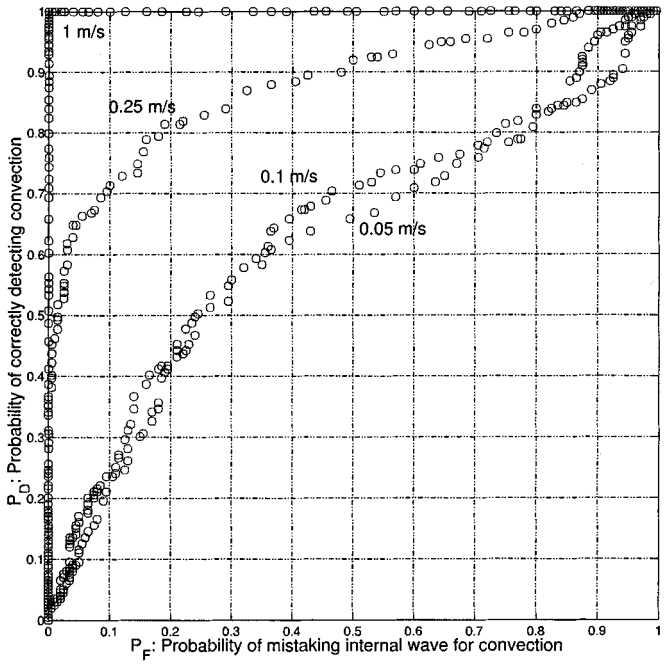

Fig. 14. Classifier's performance (P_D versus P_F) at a series of AUV speeds.

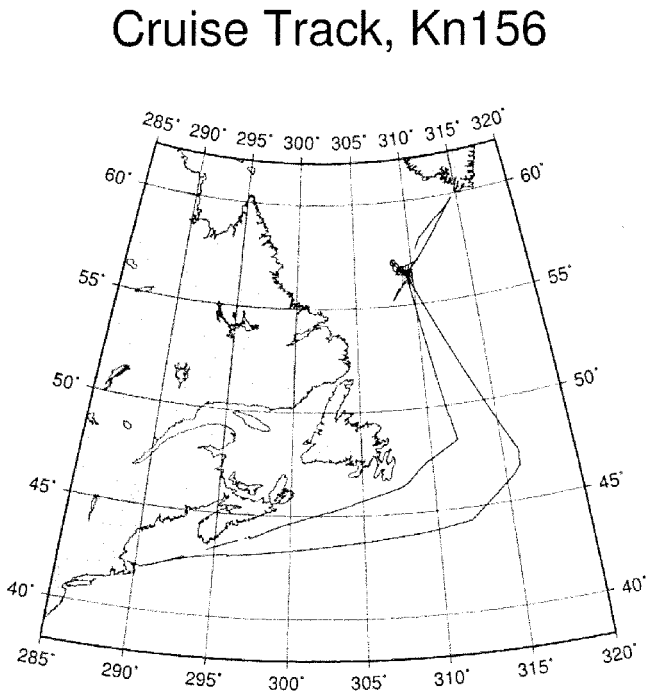

Fig. 15. Ship track of *R/V Knorr* during the 1998 Labrador Sea experiment. The focal region marks the experiment site. (Courtesy of Dr. Knut Streitlien).

change this basic spectral shape. A higher AUV speed thus pulls the peak of convection's mingled spectrum farther away from the base-frequency band where the internal wave stays despite the heightened vehicle speed. This highlighted difference improves the classifier's performance. At AUV speed of 1 m/s, the two clusters of scalar feature z do not overlap, as will be shown in Fig. 22. This indicates a even better classification performance than at AUV speed 0.25 m/s.

We have also tested the classifier's robustness by using input data that is mismatched with the model. For convection, we let the heat flux and the mixed layer depth both increase by a factor of three. This implies a significant change of the environment. As a consequence, convection's mingled spectrum gets closer to that of internal waves, making classification more challenging. Since we have incorporated model parameter uncertainty (factor of three in this case study) into the feature projection vector V in Section III-B, the classifier is prepared to the above mismatch. The classifier's performance (ROC curves omitted due to space limit) shows only a slight degradation compared with the matched case. It still holds true that a higher AUV speed better highlights convection's spatial feature so as to improve classification.

V. Labrador Sea Experiment

A. Background

The Labrador Sea lies between northern Canada and Greenland. It is one of the few locations in the world where open ocean convection occurs [23], [35]. During the winter, the sea surface is subjected to intense heat flux to the atmosphere. The resulting buoyancy loss causes the surface water to sink to large depths, initiating ocean convection.

During January/February 1998, researchers from the Massachusetts Institute of Technology, the Woods Hole Oceanographic Institution, and the University of Washington, made an expedition to the Labrador Sea to study ocean convection. The Research Vessel *(R/V) Knorr* was employed in this experiment. The map of the Labrador Sea area as well as the ship track is shown in Fig. 15 (The cruise number was KN156). AUVs and other oceanographic platforms (e.g., Lagrangian floats) were deployed in this experiment.

B. AUV-Borne Flow Velocity Measurement

We installed an ADV [36] in an Odyssey IIB AUV to measure flow velocity in the Labrador Sea. An ADV probe is illustrated in the left panel of Fig. 16. The acoustic beams of the transmitter and the three receivers intersect at a small sampling volume ($< 2\ \text{cm}^3$) located away from the instrument base (16 cm distance for Model ADVOcean we installed). Three-dimensional flow velocity at this distant focal point is calculated based on the Doppler principle. An ADV's spatial focus and low noise make it suitable for experiments that require high-resolution and high-precision [37].

With careful considerations of various installation constraints, we mounted the ADV at the AUV's largest vertical cross-section, with its probe pointing 45° from the vehicle's horizontal central plane, as shown in the right panels of Fig. 16. The ADV's three receiver tips reach the brink of the vehicle's outer fairing but do not protrude beyond it. Inside the vehicle, the ADV probe is mounted with a horizontal plate and a 45° slanted bracket. During installation, we use a laser pointer to ensure alignment accuracy.

The AUV-borne ADV measures flow velocity relative to the moving vehicle. Hence, to obtain the Earth-referenced flow velocity, i.e., the true flow velocity, we must subtract the vehicle's own velocity from the raw measurement. Another effect to re-

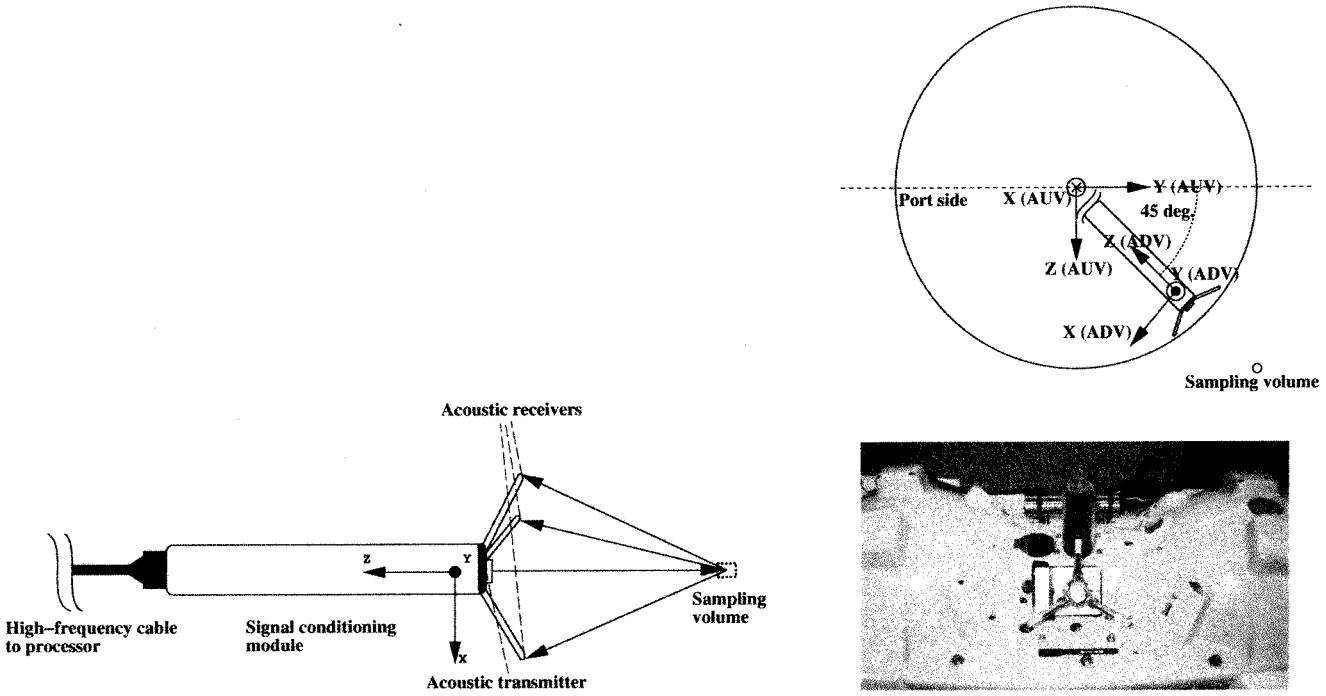

Fig. 16. Side view of an ADV probe (left), and cross-sectional view and side view of the ADV's mounting on the vehicle (right). In the upper right panel, the big circle represents the vehicle's outer fairing. In the lower right panel, the lower half of the vehicle's inner fairing is placed upside-down for ease of installation, while the outer fairing is removed.

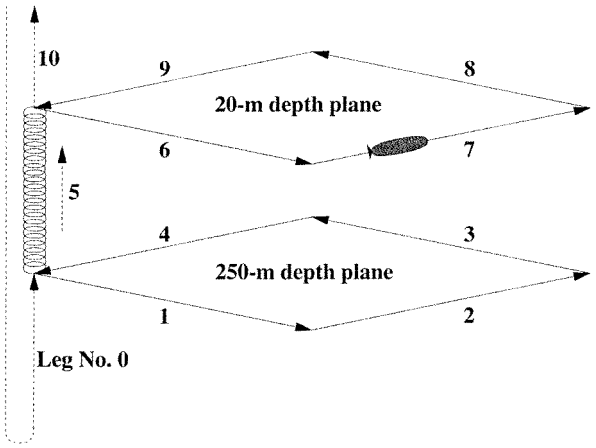

Fig. 17. AUV behavior sequence in Mission B9 804 107.

TABLE II
MEASUREMENT/ESTIMATION NOISE

Measurement/ estimation	Sensor	rms noise after 50-s smoothing
Flow velocity	ADVOcean 5 MHz	0.45 cm/s*
Heading/ attitude rate	KVH	1.4×10^{-3} rad/s
AUV vertical velocity	Paroscientific 8B-4000	0.32 cm/s
w_{Earth}		0.7 cm/s*

* For AUV mission B9804017 on the 1998 Sea Experiment.

move is the vehicle hull's influence on the measurement. To ascertain this effect, we carried out a calibration experiment in the David Taylor model basin, utilizing its large tank cross section and precise speed control of the carriage.

The Earth-referenced vertical flow velocity is extracted through the following steps [38]. 1) Transform the velocity measurement from the ADV coordinate system to the AUV coordinate system. 2) Compensate for the AUV hull's influence and subtract the velocity induced by the vehicle's rotation. 3) Recover the relative flow velocity in the Earth coordinate system using the vehicle's heading, pitch, and roll measurements. 4) Subtract the vehicle's own vertical velocity which is obtained by differentiating its depth sensor measurement. Thus the Earth-referenced vertical flow velocity is obtained.

AUV Mission B9 804 107 took place at 4:46–7:00 on February 10, 1998 (GMT). The mission launch location was about $56°42'$N, $52°46'$W, where the autonomous oceanographic sampling network (AOSN[39]) mooring was anchored. The AUV behaviors in this mission are illustrated in Fig. 17. The vehicle first spiraled down to 426-m depth, then it spiraled up to 250-m depth. At this depth plane, the vehicle made a "diamond" run, i.e., closed a four-leg loop with 90° turns, each leg lasting for 720 s. After that, it spiraled up to 20-m depth, making an identical "diamond" run. At the end, the vehicle ascended to the sea surface. The vehicle's speed in level legs was about 1 m/s.

The Earth-referenced vertical flow velocity (denoted as w_{Earth}) at the 250-m depth is extracted and shown in the first panel of Fig. 18. The vehicle's own vertical velocity (the second panel) has been removed for producing w_{Earth}. It is noted that the 250-m depth is within a 350-m mixed layer (to be shown in Section V-C).

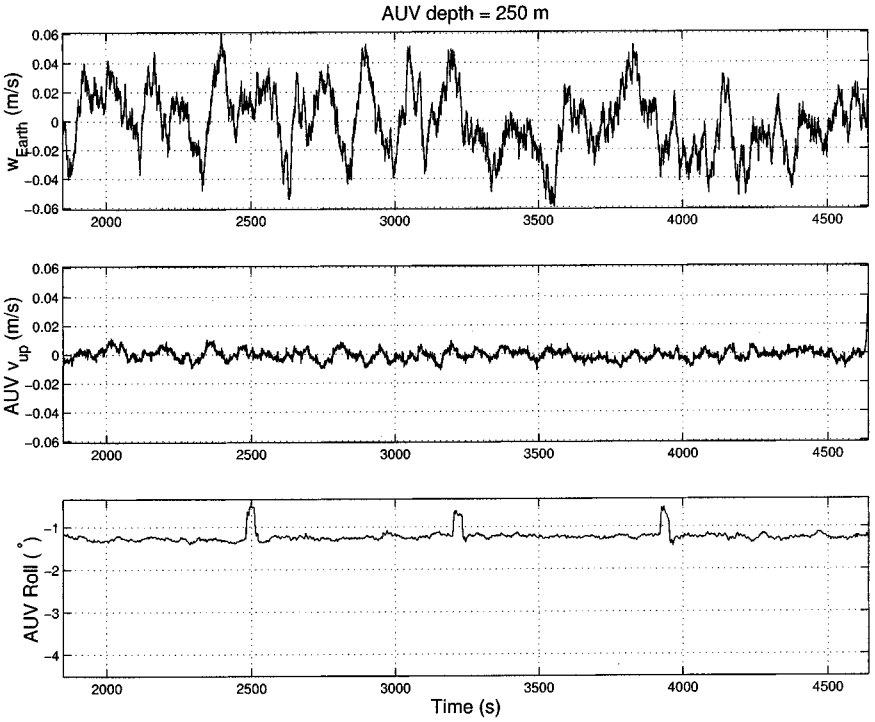

Fig. 18. The Earth-referenced vertical flow velocity w_{Earth} (the first panel) at the 250-m depth of AUV Mission B9 804 107. In the second panel is the AUV's own vertical velocity. The AUV's roll (the third panel) shows when the vehicle made 90° turns.

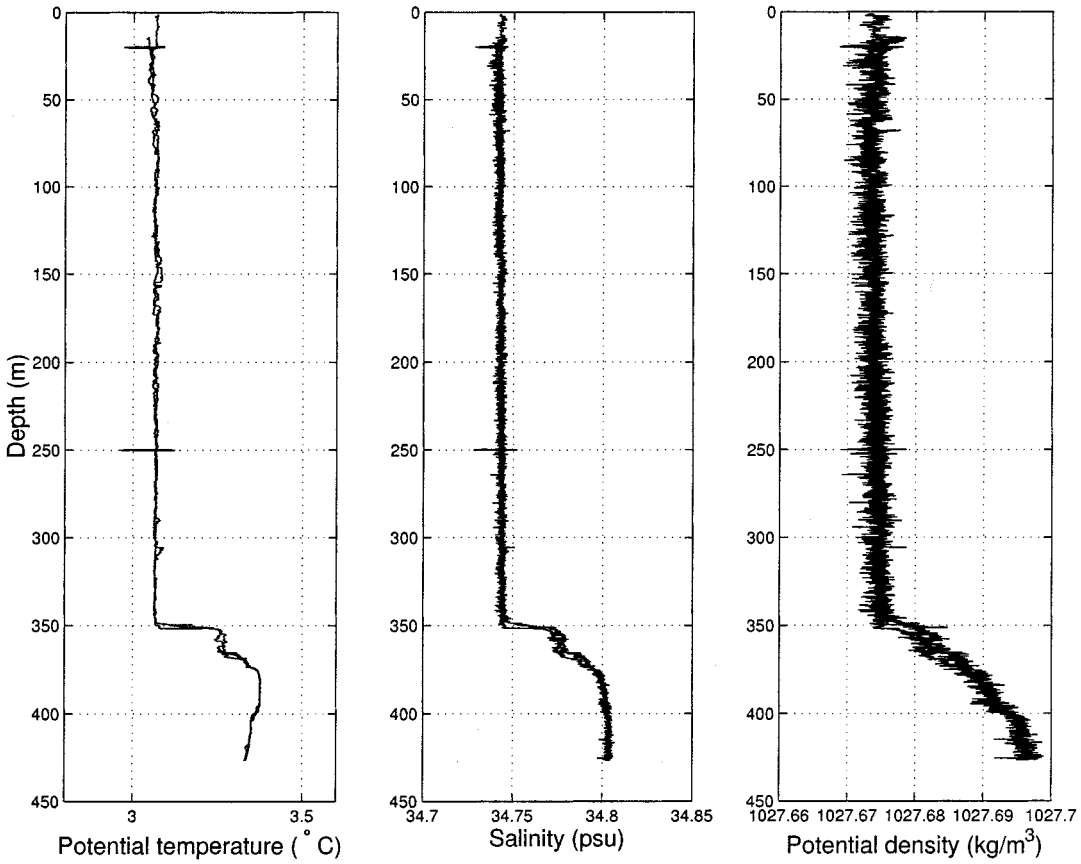

Fig. 19. Profiles of potential temperature, salinity, and potential density during AUV Mission B9 804 107.

The total noise in w_{Earth} results from three sources of measurement noise: i) ADV; ii) KVH heading/pitch/roll and rate sensor; iii) AUV's depth sensor. The source errors propagate into the final result w_{Earth} by matrix transformations in converting

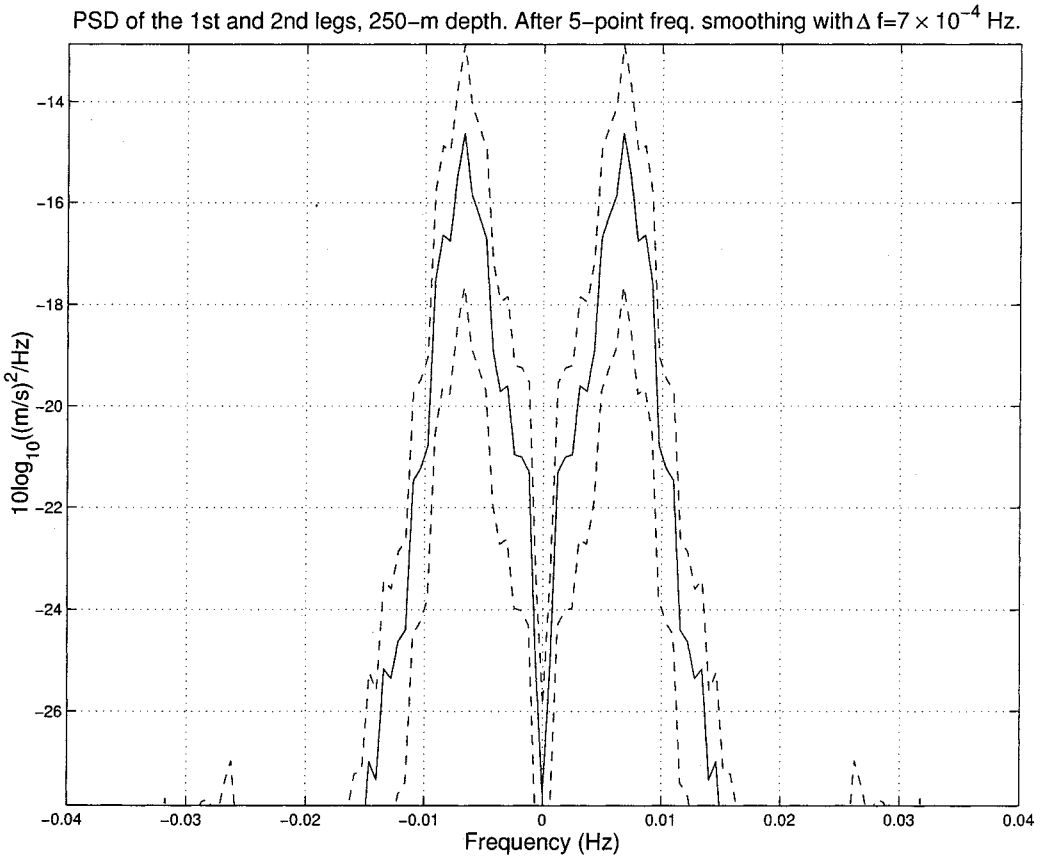

Fig. 20. PSD estimate of w_{Earth} at the 250-m depth of AUV Mission B9 804 107. Using five-point frequency-domain smoothing, the $1-\sigma$ error band is shown.

raw measurements to Earth-referenced flow velocity. Error sources and the total noise in w_{Earth} (all after 50-s smoothing) are summarized in Table II [38].

C. Test of AUV-Based Classifier by Labrador Sea Data

Meteorological data were recorded by an improved meteorological (IMET) system [40] on board *R/V Knorr*. Prof. Peter Guest of the Naval Postgraduate School calculated the ocean surface heat flux based on the measurements. During AUV Mission B9804107, the heat flux was about 300 W/m^2. Let us make comparisons with previous open ocean convection experiments. In the Greenland Sea Experiment [20] during the winter of 1988/1989, the heat flux fluctuated between 100 and 500 W/m^2, with an average value of about 250 W/m^2. Ocean convection was observed during that experiment, using moored acoustic Doppler current profilers (ADCPs). In an earlier Labrador Sea experiment [35] during the winter of 1994/1995, the average heat flux was about 300 W/m^2. Using a moored ADCP and profiling autonomous Lagrangian-circulation explorer (PALACE) floats, ocean convection was observed. The sea-surface heat flux value in our Labrador Sea Experiment is close to that of the two previous experiments. We therefore have reason to expect ocean convections occurring.

Besides surface heat loss, a vertically mixed water column is another key indicator of ocean convection. Across the Labrador Sea basin (about 600 km), a mixed water layer of depth 270 m–500 m was observed by a series of CTD casts from the ship deck (data provided by Prof. Eric D'Asaro). During two different AUV missions, mixed water layers were also clearly recorded by CTD sensors on the vehicle. During AUV Mission B9804107, the mixed layer was down to 350 m, as shown in Fig. 19. The 250-m depth plane in AUV Mission B9 804 107 is within this mixed layer.

The convection-model parameters use measurements in AUV Mission B9 804 107. Furthermore, model computations are carried out at the mission depth of 250 m. We therefore expect to see that the model-based classifier recognizes the 250-m depth w_{Earth} (shown in Fig. 18) as convection. The PSD estimate of w_{Earth} on the first and second legs is shown in Fig. 20, using five-point frequency-domain smoothing to reduce the estimation variance. We note a spectral peak at 0.007 Hz. The AUV speed during this mission was about 1 m/s. As shown in the first panel of Fig. 12, the peak frequency of the mingled-spectrum template (based on the convection model) for AUV speed 1 m/s lies at about 0.005 Hz. Those two frequencies are close.

Now let us feed the 250-m depth w_{Earth} data into the classifier. The PSD estimate of w_{Earth} is shown by the "$\triangledown$" curve in Fig. 21, along with the PSD templates of internal waves and convection. In Fig. 21, we do not conduct frequency-domain smoothing (as done in Fig. 20) to ensure that individual frequency points provide uncorrelated PSD estimates as required by the classifier's formulation. Due to the instrument noise floor, there is an upper bound of usable frequency range for classification, as given in Section IV-C. This upper bound is about 0.01 Hz at AUV speed 1 m/s, as shown in Fig. 21.

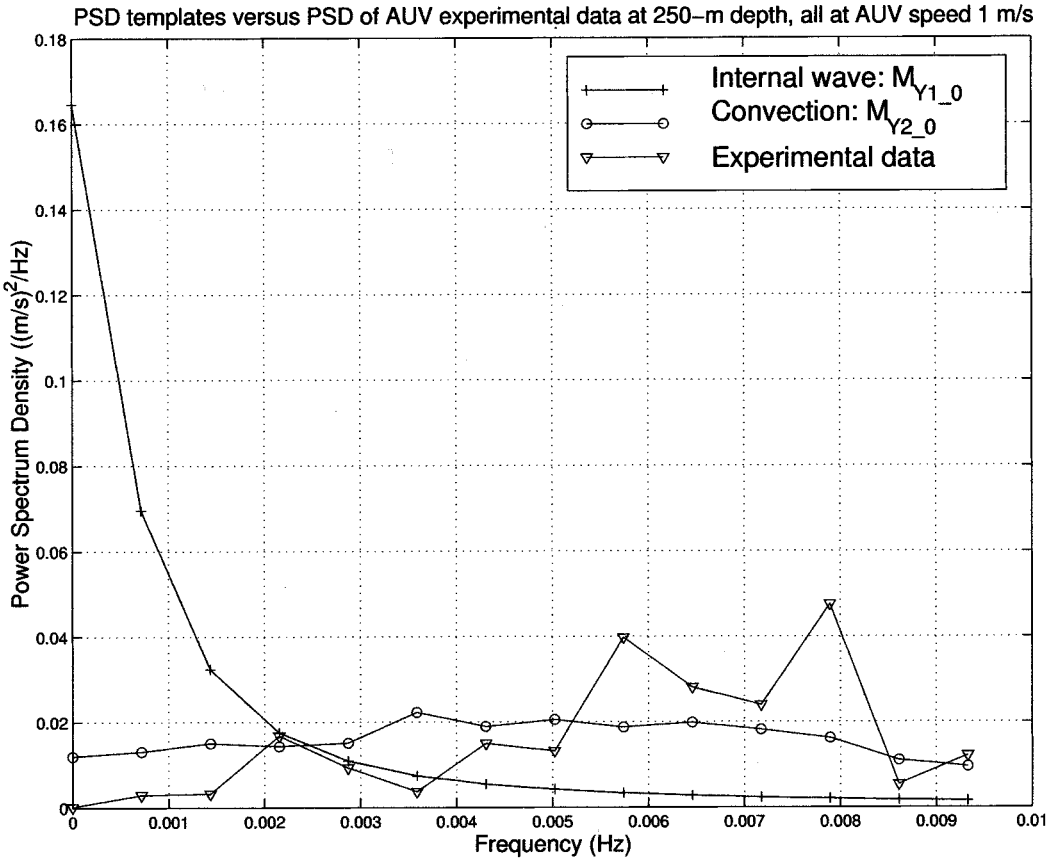

Fig. 21. PSD estimate (nonsmoothed) of w_{Earth} at the 250-m depth of Mission B9 804 107 along with PSD templates of internal wave and convection.

Using the method presented in Section III, the PSD estimate of w_{Earth} (i.e., the "∇" spectrum in Fig. 21) is transformed to a scalar feature $z_{\mathrm{experiment}}$. In the second panel of Fig. 22, the horizontal location of $z_{\mathrm{experiment}}$ is marked by an arrow. The arrow location is shown to fall in the cluster of model-based simulation results of the convection class. The classifier thus declares that the AUV-measured w_{Earth} at the 250-m depth is convective.

D. Independent Observations Supportive of Convection's Occurrence

During the same experiment, Prof. Eric D'Asaro of the University of Washington deployed seven Lagrangian floats to study convection (float design can be found in [41]). The floats' records confirm not only the existence of mixed layers, but also the occurrence of convection. Furthermore, the root-mean-square (rms) vertical flow velocity is found to be 2–3 cm/s based on the float data (calculated by Prof. Eric D'Asaro). In the 250-m depth AUV data analyzed above, the counterpart is 2 cm/s (based on the first panel of Fig. 18). Measurements by those two independent platforms are consistent.

VI. Conclusions and Discussions

A. Conclusions

We established the "mingled-spectrum principle" which concisely relates observations from a moving platform to the temporal-spatial spectrum of the process under survey. By utilizing this principle, we developed a parametric tool for designing an AUV-based spectral classifier. A test case is set up for distinguishing ocean convection from internal waves. Simulation results demonstrate that we can utilize the AUV's controllable speed to the advantage of ocean process classification.

We installed a high-precision acoustic Doppler sonar in an AUV to measure flow velocity in the Labrador Sea. Using the field data, the classifier detects convection's occurrence. This finding is supported by more traditional oceanographic analyses and observations.

B. Future Work

In the case study of convection versus internal waves, the ocean process $X(t,r)$ refers to vertical flow velocity. It is thus a scalar (as a function of time and space). To fully utilize information resources, we can add in more classification quantities, such as temperature. The addition is equivalent to expanding the dimension of process X. With dimension expansion, the mingled-spectrum computation should be correspondingly extended. Not only each component's mingled spectrum, but also cross-mingled spectra between components, will be useful for classification. A cross spectrum will reflect the correlation between two quantities. We should note, however, this correlation is based on the AUV's "mingled" measurements. The vehicle speed is still the tuning factor we should optimize for good classification.

We have considered a two-class problem, assuming knowledge of a priori spectral information about the ocean processes

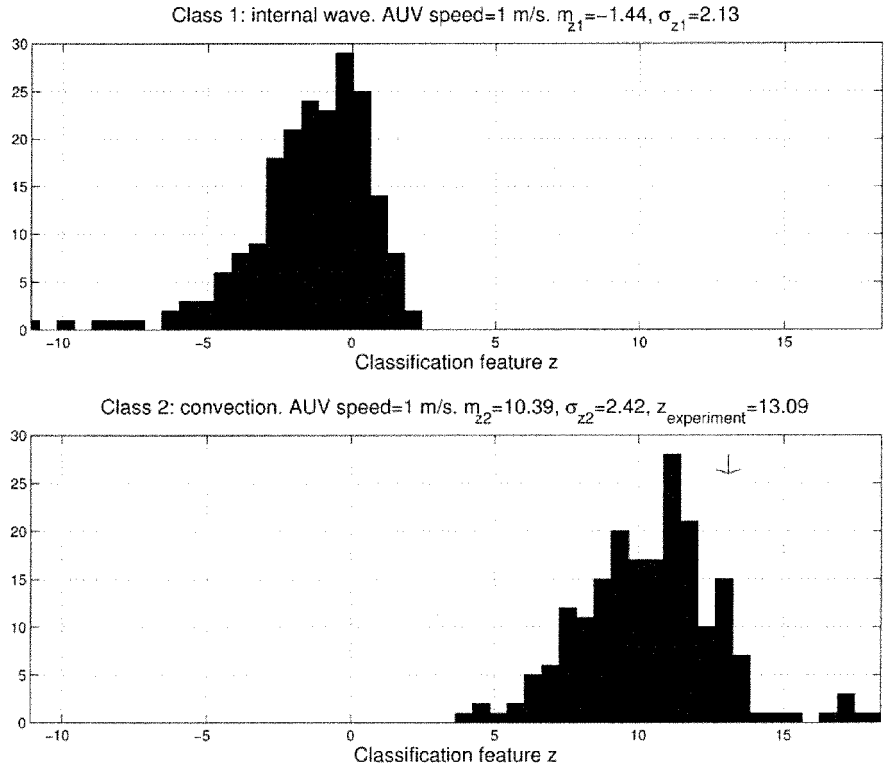

Fig. 22. At AUV speed 1 m/s, histograms of feature z for internal waves and convection. The value of $z_{\text{experiment}}$ corresponding to the 250-m depth data of AUV Mission B9 804 107 is marked by the arrow's horizontal location.

to be classified. (It is noted that while a priori information can be obtained from ocean models, new field data acquired by an AUV may improve a model through data assimilation techniques [42].) In distinguishing convection from internal waves, the binary hypothesis formulation is plausible, as the former process occurs mainly in a vertically mixed water column while the latter occurs in a stably stratified water column. When there are more possible ocean processes, we need to extend the binary classification method to *M*-ary [16] $(M > 2)$ classification. The class separability metric is readily extendible to M-class problems [17]. Correspondingly, feature extraction will map the observation vector to an $(M-1)$-dimension feature vector Z. For a two-class problem where $M = 2$, vector Z reduces to a scalar feature z, as seen in the paper.

ACKNOWLEDGMENT

The authors would like to thank WHOI Senior Scientist Dr. A. Williams III for his important help in the Labrador Sea Experiment data processing and analysis; ONR Program Manager Dr. T. Curtin and MIT Sea Grant Director Prof. C. Chryssostomidis for their support; Prof. J. Marshall and Dr. H. Hill for providing the MIT ocean convection model; Prof. P. Guest of the Naval Postgraduate School, Prof. E. D'Asaro, and Ms. E. Steffen of the University of Washington for sharing their Labrador Sea meteorological and floats data; MIT Sea Grant AUV Lab staff Dr. K. Streitlien, Dr. B. Moran, Dr. J. Bales, and Mr. R. Grieve for their help during experiments; WHOI Scientists Dr. J. Colosi and Dr. J. Preisig for suggestions; Prof. W. Munk of the Scripps Institution of Oceanography, Prof. C. Wunsch of MIT, and the three reviewers, for their beneficial comments; and Dr. A. Williams III and MIT Prof. J. Leonard from the Ph.D. thesis committee for their guidance to the first author.

REFERENCES

[1] J. G. Bellingham, "New oceanographic uses of autonomous underwater vehicles," *Mar. Technol. Soc. J.*, vol. 31, no. 3, pp. 34–47, 1997.
[2] W. J. Emery and R. E. Thomson, *Data Analysis Methods in Physical Oceanography*. New York: Elsevier, 1998.
[3] G. L. Pickard and W. J. Emery, *Descriptive Physical Oceanography: An Introduction*. New York: Pergamon, 1990.
[4] P. K. Kundu, *Fluid Mechanics*. London, U.K.: Academic, 1990.
[5] F. Bahr and P. D. Fucile, "SeaSoar—A flying CTD," *Oceanus*, vol. 38, no. 1, pp. 26–27, 1995.
[6] F. P. Bretherton, R. E. Davis, and C. B. Fandry, "A technique for objective analysis and design of oceanographic experiments applied to MODE-73," *Deep-Sea Res.*, vol. 23, pp. 559–582, 1976.
[7] J. G. Bellingham and J. S. Willcox, "Optimizing AUV oceanographic surveys," in *Proc. IEEE Symp Autonomous Underwater Vehicle Technology*, Monterey, CA, June 1996, pp. 391–398.
[8] P. A. Matthews, "The impact of nonsynoptic sampling on mesoscale oceanographic surveys with towed instruments," *J. Atmos. Ocean. Technol.*, vol. 14, no. 1, pp. 162–174, 1997.
[9] C. Wunsch, *The Ocean Circulation Inverse Problem*. Cambridge, U.K.: Cambridge Univ. Press, 1996.
[10] A. D. Voorhis and H. T. Perkins, "The spatial spectrum of short-wave temperature fluctuations in the near-surface thermocline," *Deep-Sea Res.*, vol. 13, pp. 641–654, 1966.
[11] C. Garrett and W. Munk, "Internal waves in the ocean," *Annu. Rev. Fluid Mech.*, vol. 11, pp. 339–369, 1979.
[12] D. B. Percival and A. T. Walden, *Spectral Analysis for Physical Applications*. Cambridge, U.K.: Cambridge Univ. Press, 1993.
[13] D. E. Dudgeon and R. M. Mersereau, *Multidimensional Digital Signal Processing*. Englewood Cliffs, NJ: Prentice-Hall, 1984.
[14] Y. Zhang, "Spectral feature classification of oceanographic processes using an autonomous underwater vehicle," Ph.D. dissertation, Dept. Ocean. Eng., Massachusetts Institute of Technology and Woods Hole Oceanographic Institution, 2000.
[15] C. Garrett and W. Munk, "Space–time scales of internal waves," *Geophys. Fluid Dyn.*, vol. 2, pp. 225–264, 1972.

[16] H. L. Van Trees, *Detection, Estimation, and Modulation Theory*. New York: Wiley, 1968, pt. I.
[17] K. Fukunaga, *Introduction to Statistical Pattern Recognition*, 2nd ed. New York: Academic, 1990.
[18] A. V. Oppenheim and R. W. Schafer, *Discrete-Time Signal Processing*. Englewood Cliffs, NJ: Prentice-Hall, 1989.
[19] G. M. Jenkins and D. G. Watts, *Spectral Analysis and its Applications*. San Francisco, CA: Holden-Day, 1968.
[20] F. Schott, M. Visbeck, and J. Fischer, "Observations of vertical currents and convection in the central Greenland Sea during the winter of 1988–1989," *J. Geophys. Res.*, vol. 98, no. C8, pp. 14 401–14 421, 1993.
[21] F. Schott, M. Visbeck, U. Send, J. Fischer, L. Stramma, and Y. Desaubies, "Observations of deep convection in the Gulf of Lions, Northern Mediterranean, during the winter of 1991/92," *J. Phys. Oceanogr.*, vol. 26, no. 4, pp. 505–524, 1996.
[22] H. D. Young, *University Physics*. Reading, MA: Addison-Wesley , 1992.
[23] J. Marshall, "The Labrador Sea deep convection experiment," *Bull. Amer. Meteorol. Soc.*, vol. 79, no. 10, pp. 2033–2058, 1998.
[24] E. D'Asaro, "Measuring Deep Convection, Workshop Rep.," Applied Physics Lab., University of Washington, Seattle, WA, 1994.
[25] M. S. McCartney, "Oceans and climate: The ocean's role in climate and climate change," *Oceanus*, vol. 39, no. 2, pp. 2–3, 1996.
[26] H. Jones and J. Marshall, "Convection with rotation in a neutral ocean: A study of open-ocean convection," *J. Phys. Oceanogr.*, vol. 23, no. 6, pp. 1009–1039, 1993.
[27] B. A. Klinger and J. Marshall, "Regimes and scaling laws for rotating deep convection in the ocean," *Dyn. Atmos. Oceans*, vol. 21, pp. 227–256, 1995.
[28] J. N. Newman, *Marine Hydrodynamics*. Cambridge, MA: MIT Press, 1977.
[29] J. R. Apel, *Principles of Ocean Physics*. London, U.K.: Academic, 1987.
[30] J. A. Colosi and M. G. Brown, "Efficient numerical simulation of stochastic internal-wave-induced sound-speed perturbation fields," *J. Acoust. Soc. Amer.*, vol. 103, no. 4, pp. 2232–2235, 1998.
[31] C. Garrett and W. Munk, "Space–time scales of internal waves: A progress report," *J. Geophy. Res.*, vol. 80, no. 3, pp. 291–297, 1975.
[32] W. Munk, "Internal waves and small-scale processes," in *Evolution of Physical Oceanography: Scientific Surveys in Honor of Henry Stommel*, B. A. Warren and C. Wunsch, Eds. Cambridge, MA: MIT Press, 1981, pp. 264–291.
[33] H. V. Poor, *An Introduction to Signal Detection and Estimation*, 2nd ed. New York: Springer-Verlag, 1994.
[34] S. M. Kay, *Modern Spectral Estimation: Theory and Application*. Englewood Cliffs, NJ: Prentice-Hall, 1998.
[35] J. M. Lilly, P. B. Rhines, M. Visbeck, R. Davis, J. R. N. Lazier, F. Schott, and D. Farmer, "Observing deep convection in the Labrador Sea during winter 1994/95," *J. Phys. Oceanogr.*, vol. 29, no. 8, pp. 2065–2098, 1999.
[36] *Acoustic Doppler Velocimeter (ADV) Operation Manual (Firmware Version 4.0)*, SonTek, San Diego, CA, June 1997.
[37] A. J. Williams III, "Historical overview: Current measurement technologies," *IEEE Oceanic Eng. Soc. Newslett.*, pp. 5–9, Spring 1998.
[38] Y. Zhang, K. Streitlien, J. G. Bellingham, and A. B. Baggeroer, "Acoustic Doppler velocimeter flow measurement from an autonomous underwater vehicle with applications to deep ocean conversion," *J. Atmos. Oceanic Eng.*, vol. 18, no. 12, 2001.
[39] T. Curtin, J. G. Bellingham, J. Catipovic, and D. Webb, "Autonomous oceanographic sampling network," *Oceanography*, vol. 6, no. 3, pp. 83–94, 1993.
[40] D. S. Hosom, R. A. Weller, R. E. Payne, and K. E. Prada, "The IMET (Improved METeorology) ship and buoy systems," *J. Atmos. Oceanic Eng.*, vol. 12, no. 3, pp. 527–540, 1995.
[41] E. A. D'Asaro, D. M. Farmer, J. T. Osse, and G. T. Dairiki, "A Lagrangian float," *J. Atmos. Oceanic Technol.*, vol. 13, pp. 1230–1246, 1996.
[42] A. R. Robinson, P. F. J. Lermusiaux, and N. Q. Sloan, "Data Assimilation," in *The Sea: The Global Coastal Ocean*, K. H. Brink and A. R. Robinson, Eds. New York: Wiley, 1998, vol. 10.

Yanwu Zhang (S'95–M'00) was born in June 1969 in Shaanxi Province, China. He received the B.S. degree in electrical engineering, the M.S. degree in underwater acoustics engineering, from Northwestern Polytechnic University, Xi'an, China, in 1989 and 1991, respectively, the M.S. degree in electrical engineering and computer science from the Massachusetts Institute of Technology (MIT), Cambridge, MA, in 1998, and the M.S. and Ph.D. degrees in oceanographic engineering from the MIT/Woods Hole Oceanographic Institution (WHOI) Joint Program, in 2000.

From June to December 2000, he was a Systems Engineer working on medical image processing at the General Electric Company Research and Development Center, Niskayuna, NY. Since January 2001, he has been a Digital Signal Processing (DSP) Engineer in the Research and Development Division of Aware Inc., Bedford, MA, working on digital communications. His research interests are in spatio-temporal signal processing, autonomous-underwater vehicles, and digital communications.

Dr. Zhang is a member of Sigma Xi.

Arthur B. Baggeroer (S'62–M'68–SM'87–F'89) received the B.S.E.E. degree from Purdue University, West Lafayette, IN, in 1963, and the Sc.D. degree from the Massachusetts Institute of Technology (MIT), Cambridge, MA, in 1968.

He is a Ford Professor of Engineering in the Department of Ocean Engineering and the Department of Electrical Engineering and Computer Science at MIT. He has also been a consultant to the Chief of Naval Research at the NATO SACLANT Center in 1977 and a Cecil and Ida Green Scholar at the Scripps Institution of Oceanography in 1990 while on sabbatical leaves. His research has been concerned with sonar array processing, acoustic telemetry, and most recently, global acoustics and matched field array processing. He also has had a long affiliation with the Woods Hole Oceanographic Institution (WHOI) and was Director of the MIT/WHOI Joint Program from 1983 to 1988.

Dr. Baggeroer is a Fellow of the Acoustical Society of America, and he was elected to the National Academy of Engineering in 1995. He was awarded the Secretary of the Navy/Chief of Naval Operations Chair in Oceanographic Science in 1998.

James G. Bellingham received the M.S., and Ph.D. degrees in physics, from the Massachusetts Institute of Technology (MIT), Cambridge, MA, in 1984, and 1988, respectively.

He spent the last thirteen years developing Autonomous Underwater Vehicles (AUV), first as Manager of the MIT Sea Grant College Program AUV Laboratory and, more recently, as the Director of Engineering at the Monterey Bay Aquarium Research Institute (MBARI), Moss Landing, CA. He has worked in areas ranging from vehicle design, to high-level control, to field operations. His primary contribution is the creation of the Odyssey class of AUVs with which he has led operations in areas as remote as the Arctic and Antarctic. In the area of high-level control, he developed state-configured layered control, a new methodology for handling mission-level control of autonomous vehicles.

Dr. Bellingham is a founder and member of the Board of Directors of Bluefin Robotics Corporation, a leading manufacturer of AUVs for the military, commercial, and scientific markets.